Mechanics of Time-Dependent Materials (2025) 29:72
https://doi.org/10.1007/s11043-025-09801-z

RESEARCH

Prediction of creep behavior in short fiber reinforced polymer matrix composites using an elementary volume approach

J. Rech[1,2,3] · B. Möginger[1] · H.C. Ludwig[4] · B. Hausnerova[2,3]

Received: 10 February 2025 / Accepted: 25 June 2025 / Published online: 8 August 2025

Abstract

Creep behavior of short glass fiber reinforced poly(butylene terephthalate) (SFRC PBT) composites was analyzed using plates processed by injection molding and push–pull processing, with fiber contents of 0, 20, and 30 wt%. Tensile test bars were extracted parallelly and perpendicularly to the flow direction to assess short-term mechanical properties, fiber length distribution, and orientation. An elementary volume approach was used to predict the longitudinal and transverse creep compliances, showing that the time dependencies were mainly governed by the PBT matrix. Given the minimal fiber orientation in the thickness direction, a transformation based on RM Jones' mechanics of composite materials was applied to account for fiber misalignment. This led to the introduction of the unknown shear modulus G_{12}, which was addressed by expressing it in terms of the transverse compliance J_{22} and shear correction factor. Comparison of predicted and measured creep compliances revealed an underestimation of 15–30% parallelly and 5–15% perpendicularly to the flow direction, attributed to imperfect fiber-matrix adhesion. SEM analysis of fracture surfaces indicated different failure behaviors based on the fiber orientation. This suggests that fiber-matrix adhesion is stress-direction dependent. The time range for accurate prediction of composite creep behavior, governed by matrix creep, is defined by the creep time limit, which decreases exponentially with increasing creep stress.

Keywords Modeling · Creep compliance · Polymer matrix composite · Short fiber reinforcement · Fiber aspect ratio distribution · Fiber orientation distribution · Shear correction factor · Creep time limit

✉ B. Hausnerova
hausnerova@utb.cz

1 Bonn-Rhein-Sieg University of Applied Sciences, von-Liebig-Straße 20, 53359 Rheinbach, Germany

2 Centre of Polymer Systems, University Institute, Tomas Bata University in Zlin, nam. T.G. Masaryka 5555, 76001 Zlin, Czech Republic

3 Faculty of Technology, Tomas Bata University in Zlin, Vavreckova 275, 76001 Zlin, Czech Republic

4 Ingenieurbüro Ludwig, Groenen Feld 29, 49328 Melle, Germany

1 Introduction

Neat thermoplastics often do not meet the technical requirements of mass-produced injection-molded parts for elevated applications. To overcome such restrictions and open new application fields, thermoplastics are reinforced by short fibers to enhance stiffness, strength, and shape stability at elevated temperatures and to reduce creep under external loads. However, the introduction of short fibers causes drawbacks, for example, reduction of toughness or anisotropic mechanical and thermal material properties owing to a preferential fiber orientation distribution introduced by local flow conditions during mold filling.

Even for continuous-fiber-reinforced parts, it is not always possible to align the fiber and load directions. The calculation of relevant material properties requires transforming the stiffness or compliance tensors due to the misalignment of the fiber and load directions (Jones 1975). In the case of short fiber-reinforced composites (SFRC), the transformation can be performed using orientation tensors combined with orientation averaging to account for locally varying fiber orientations (Tucker and Liang 1999).

Obviously, the properties $P_{\text{composite}}$ of the SFRC composite depend on the properties of the matrix P_{matrix}, fibers P_{fiber}, fiber volume content v_{F}, aspect ratio distribution $\langle r \rangle$, fiber orientation distribution (A), and fiber matrix adhesion k_{adh} (Chin et al. 1988; Fu 1996). When it comes to modeling and predicting the properties, all these quantities have to be taken into account, leading to a manifold of models. For practitioners, the most popular model because of its simplicity is the semiempirical Halpin–Tsai model (Halpin and Kardos 1976) derived from the self-consistent models of Hermans (1967) and Hill (1964):

$$P_{\text{composite}} = P_{\text{matrix}} \frac{1 + \xi \eta v_{\text{F}}}{1 - \eta v_{\text{F}}} \quad \text{with} \quad \eta = \frac{\frac{P_{\text{matrix}}}{P_{\text{fiber}}} - 1}{\frac{P_{\text{matrix}}}{P_{\text{fiber}}} + \xi}. \tag{1}$$

However, to account for any given preferential fiber orientation, they had to introduce an efficiency factor ξ, which had to be determined empirically for fiber orientations not aligning the main axes.

The first concise treatment of SFRC was performed by Eshelby (1957), who considered the effects of a single ellipsoidal inclusion in an infinite body on the components of the stiffness or compliance tensor. Tandon and Weng (1984) combined Eshelby's solutions with the average stress concept of Mori and Tanaka (1973) and calculated the components of the stiffness tensor for transversely isotropic composites assuming isotropic inclusions, such as glass beads or glass fibers. Qiu and Weng (1990) extended this model to transversely isotropic inclusions, such as carbon fibers. Both models depend on Eshelby's tensor elements and the Lamé constants of the matrix and fibers in a complex manner, but work well for composites containing fibers, spherical or arbitrarily shaped particles, and platelets (Lusti 2003; Rauter and Lammering 2020).

Finite element methods were developed by Gusev (1997, 2001) to predict the properties of multiphase materials based on 3D periodic multiinclusion computer models. The application of periodic boundary conditions allows the prediction of the properties of composites using small computer models. A *unit cell* or minimal *representative volume element* (RVE) comprising 25 spheres is representative of particle-filled composites with random microstructures. For SFRC, an RVE comprising 100 parallel fibers is necessary for accurate predictions of longitudinal Young's moduli E_{11} (Lusti 2003). Breuer and Stommel (2020) investigated how RVE with varying fiber volume content, fiber shape, aspect ratio, and fiber orientation distribution affect the predicted composite stiffness and compared them to the

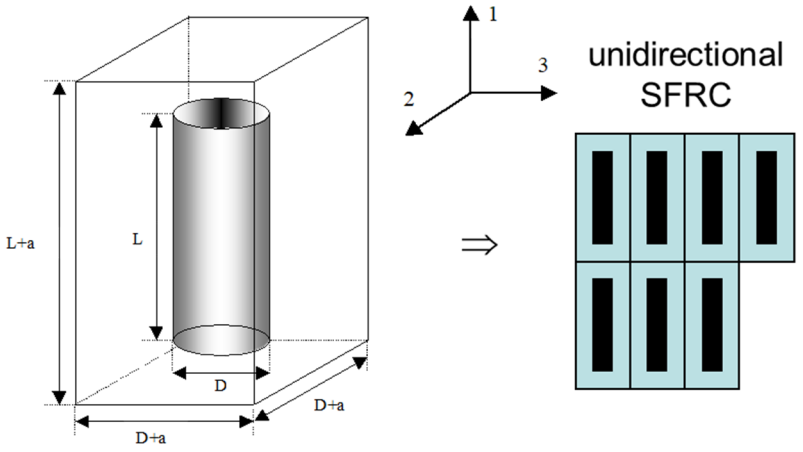

Fig. 1 Elementary volume containing a single fiber of length L and diameter D with distance a to the neighboring fiber (left) and the formation of unidirectional SFRC (right) (Color figure online)

stiffness of 20 wt% glass fiber reinforced poly(butylene terephthalate) (PBT GF20). It is important to note that the aspect ratio input has significant effects: the arithmetic mean aspect ratio provides $E = 6{,}500$ MPa, and the aspect ratio distribution provides $E = 7,600$ MPa. This shows that longer fibers contribute more to the composite stiffness. Furthermore, cylindrical fibers provide composites with a higher stiffness than ellipsoidal inclusions with the same aspect ratio.

In elementary volume approaches, an *elementary volume* (EV) containing a single fiber of length L represents the ultimate properties of composites with respect to the main axes (Möginger et al. 1999; Wilczynski 1990; Wire et al. 1999). All these approaches yield a significant dependency of the longitudinal moduli on the aspect ratio, whereas the transverse moduli decrease slightly. In the simplest case, the neighboring fibers have a distance a in each direction. This leads to a square column-shaped EV of length $L + a$, width $D + a$, and thickness $D + a$. Thus the regular 3D lattice arrangement of the EV can form an infinite unidirectional transversal isotropic SFRC, Fig. 1. To derive the ultimate components of the stiffness tensor, EV is divided into a matrix part and a composites part, and the stress and strain are calculated for both parts. A comparison of the stress and strain of EV provides the components of the stiffness tensor that depend only on the properties of both the matrix and fibers, fiber volume content, aspect ratio, and geometry constant k taking into account the shape of the inclusion. A comparison of the components of the stiffness tensor of the Halpin–Tsai, Tandon–Weng, and EV models is provided in Appendix A.

The aforementioned models provide a toolbox that allows the prediction of static mechanical properties with respect to a predefined accuracy level. The prediction of the creep behavior of SFRC is much more challenging, as on one hand, matrix inhomogeneities, fiber orientation distribution (FOD), fiber lengths degradation may generate different time-dependent creep contributions. On the other hand, increasing the crystallinity of neat PBT from 30% to 36% did not alter the Young moduli and tensile strengths within the accuracy of measurement but significantly affected the creep behavior (Möginger 1992). Sakai et al. (2018) investigated the effects of crystallinity on the creep behavior of SFRC of PA66 and found little effect on the moduli but significant effects on creep compliances.

Currently, three approaches are used to model the creep behavior of SFRC. The first is to measure creep compliances and fit the data with appropriate empirical or viscoelastic

Table 1 Some models of time and stress-dependent creep compliances $J(t, \sigma_0)$

Models	Creep strain/Creep compliance
Burgers	$J(t,\sigma_0) = \left(\frac{1}{E_1} + \frac{1}{E_2}\left(1 - e^{-\frac{E_2}{\eta_2}t}\right) + \frac{t}{\eta_1}\right)$ (2) with time t, initial stress σ_0, stiffnesses of Burgers model E_1, E_2, and viscosities of Burgers model η_1, η_2
Modified Burgers	$J(t,\sigma_0) = \left(\frac{1}{E_1} + \frac{1}{E_2}\left(1 - e^{-\frac{t}{(a\tau^b)}}\right) + \frac{t}{\eta_1}\right)$ (3) with relaxation time τ and fitting parameters a and b
Findley power law	$J(t,\sigma_0) = \frac{\varepsilon_0}{\sigma_0} + \frac{\varepsilon^+}{\sigma_0}t^n = \frac{1}{E_1} + \frac{\varepsilon^+}{\sigma_0}\left(\frac{t}{t_1}\right)^n$ (4) with initial strain ε_0, transient strain ε^+, exponent n, and reference time t_1
Findley modified power law	$J(t,\sigma_0) = \frac{\varepsilon_0}{\sigma_0}\sinh\left(\frac{\sigma_0}{\sigma_1}\right) + \frac{\varepsilon^+}{\sigma_0}t^n \sinh\left(\frac{\sigma_0}{\sigma_1}\right)$ (5) with reference stress σ_1
Bailey-Norton	$J(t,\sigma_0) = A\sigma_0^{m-1}\left(\frac{t}{t_1}\right)^{n^+}$ (6) with coefficient A and exponents m and n^+
Power series	$J(t,\sigma_0) = J_0 + \sum_{i=1}^{m} J_i\left(\frac{t}{t'}\right)^i$ (7) with reference time t', relaxation strengths J_i, and index i
Prony–Dirichlet series	$J(t,\sigma_0) = J_0 + \sum_{i=1}^{m} J_i\left(1 - e^{\left(-\frac{t}{\tau_i}\right)}\right)$ (8) with relaxation times τ_i

models Ediger (1986), Table 1. The functions of these models define the general time and/or stress dependency, and the coefficients define the material-specific creep behavior under the given test conditions.

In all cases, it is a "retrospective" modeling: the experimental creep data are fitted by one of the above-listed models, equations (2)–(8). This is a reasonable approach if the long-term behavior of parts must be simulated by finite element analysis (FEA) with the input of material functions via the fit parameters of the models. However, a general prediction of the creep behavior of SFRC is difficult because it depends on the varying FOD in the parts. However, the FOD may vary strongly with the processing parameters and local flow conditions in the mold, even for the same SFRC. Because the FOD is implicitly included in the model parameters, it must be determined by creep measurements in each case.

The second is to predict the long-term creep behavior using creep models fed by short-term creep data. Naumann and Stommel (2012) developed a stress- and temperature-dependent creep model based on the free-volume approach. They successfully applied it to creep data of neat polymers PC, PMMA, PP, PC/ABS, and POM determined by an Iosipescu shear device for up to 10,000 h. Lim et al. (2004) developed a power law-based creep model. It required the division of the short-term creep test into six time regions (0.2, 1, 5, 25, 100,

and 300 h) and determined the corresponding hardening time creep parameters for each region, which were subsequently used for creep predictions of injection-molded bars of ABS, ABS/PC, and long fiber thermoplastics (LFT) at 80 °C. However, the effects of FOD have not been directly considered.

Gates et al. (1996) investigated the physical aging behavior of continuous carbon fiber-reinforced polyimide in terms of creep compliance. They established an analytical model capable of predicting the long-term creep behavior based on short-term creep data. A comparison of the measured creep curves showed that shear creep was predicted more accurately than transverse creep.

Zhang et al. (2021) fitted the short-term data of short carbon fiber-reinforced PEI with four viscoelastic models and checked them for accuracy and efficiency. They then applied time-temperature superposition (TTS) to predict long-term creep behavior. The generated master curve reproduced the data in an unsatisfactory manner and clearly showed that TTS cannot be applied to two-phase systems with FOD.

Duan et al. (2021) developed a unified phenomenological creep model for particle-filled composites containing three temperature- and stress-dependent fit parameters in the exponential function to address all three creep stages. They used creep data of a fluoro-rubber filled with 94 wt% $BaSO_4$ particles measured at different temperatures and stresses, as well as third-party measurements of high-density polyethylene (Amjadi and Fatemi 2021) for verification purposes. The model partly reproduced the creep data well and was capable of predicting rupture times.

Katouzian et al. (2023) reviewed currently used models such as the micromechanical model, Mori–Tanaka method, homogenization techniques, and FEA with respect to the capability to predict the creep of unidirectional carbon fiber-reinforced composites and found that all methods are appropriate prediction tools. In particular, they considered FEA to be a very promising method to reduce the number of costly creep experiments.

Dean et al. (2008) measured the tensile creep strains of POM and modeled them using a four-parameter function. One parameter related to the mean retardation time for the relaxation process decreases with increasing stress, which leads to a nonlinear creep behavior. Creep measurements under compression and shear enabled the model to account for different stress states. The implementation of FEA allowed for good creep predictions under stepwise stress variations.

The third is to implement the viscoelastic behavior of the matrix in a microstructural FE model to predict the creep behavior of SFRC. Fliegener et al. (2016) introduced the principal matrix creep behavior using the Burgers model and assumed perfect fiber-matrix adhesion. Then they verified the microstructure FE model with creep data of long-fiber-reinforced PP with fiber weight contents of 10, 20, and 30% over one week at several stress levels. All the calculated creep curves exhibited a correct time dependency but at somewhat reduced creep strains.

Zhai et al. (2018) developed a phenomenological visco-plastic model considering damage generation expressed by a damage variable. They verified the model on the creep data of quasi-unidirectional PP composites by performing off-axis measurements. Their model also underpredicted the measured creep strains, but still in a satisfactory manner. From a material scientific point of view, a good model must predict smaller creep compliances if perfect fiber-matrix adhesion is assumed.

The goal of this study is to demonstrate that the measured matrix creep is sufficient to predict the reasonable creep compliance of SFRC if introduced in a semiempirical EV model that also considers the fiber orientation distribution (FOD) and fiber length distribution (FLD).

Table 2 Investigated PBT composites with moduli according to manufacturers' data sheets (BASF)

Material	Trade names	Weight content w_F (GF) %	Volume content v_F (GF) %	Young's modulus* E MPa
PBT, neat	Vestodur 2000	0	0	2,600
PBT GF20	Ultradur B4300 G4	20	0.09	7,000
PBT GF30	Ultradur B4300 G6	30	0.13	9,700
GF	-	-	-	74,000

*Determined using test bar type A according to ISO 3167 (Campus test bar)

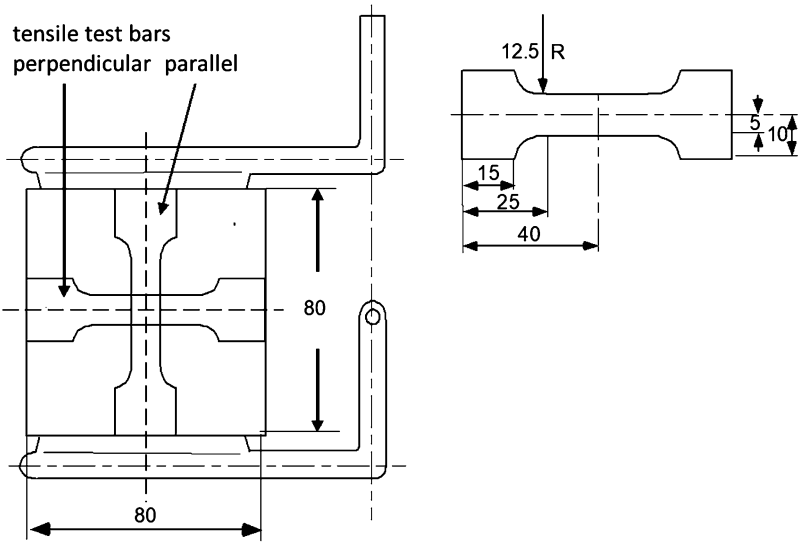

Fig. 2 Geometry of the injection molded rectangular plates having dimensions 80 × 80 × 2.5 mm^3 (left) and the tensile test bars (right)

2 Materials and methods

2.1 Materials

The investigations were performed using poly(butylene terephthalate) (PBT) reinforced with short glass fibers (GF), Table 2.

The PBT compounds were processed by a two-component injection molding machine Ferromatik Milacron FM F 110 S/2F to plates of length 80 mm, width 80 mm, and thickness of 2.5 mm, Fig. 2 (left). From each of these plates, three test bars were removed parallelly to the flow direction and perpendicularly to it. The geometry of the test bar is shown in Fig. 2 (right). The plates were manufactured using conventional injection molding (CIM) and push–pull processing (PPP) (Ludwig 1998) to introduce different cross-sectional fiber orientation distributions.

2.2 Methods

2.2.1 Determination of mean fiber length and orientation

The granules and small central parts of the plates were heated to 950 °C at a heating rate of 20 K/min in a Mettler Toledo TGA/SDTA 851 to pyrolyze the matrix. The remaining glass fibers were individually distributed in a glass dish. The lengths of a few 100 fibers were measured by image analysis to determine the mean fiber lengths and aspect ratios. To determine the fiber orientation, sections were cut from the plate. After embedding in epoxy resin and polishing the cross-section, the fiber ellipses were evaluated using the section method to determine the inclination angles θ and plane angles ϕ. These angles allowed for the calculation of the spatial orientation of the fibers. Averaging over the sample cross-section provided the mean orientation factors f_1, f_2, and f_3.

2.2.2 Tensile tests

Tensile tests were performed using a universal testing machine Zwick 1476 with a strain rate of 10%/min at 23 °C and 50% r.h. and 5 repetitions ($n = 5$). The stress–strain curves were evaluated according to ISO 527 to determine the Young modulus, tensile strength, and elongation at break.

2.2.3 Creep tests

Creep tests were performed for 336 h (two weeks) at 23 °C and 50% r.h. according to ISO 899-1 in the creep stand Zwick 4211 with fully automated data acquisition (Pöllet 1985). The initial stresses σ_0 were chosen to be 12.5 MPa, 25 MPa, and 37.5 MPa, corresponding to 25%, 50%, and 75% of the yield stress σ_{yield} of neat PBT. The measured creep strain curves $\epsilon(t)$ had to be corrected with respect to the initial strain ϵ_0 because the initial length L_0 was measured in the unloaded state. During loading, the test bars may slide vertically in the clamps, and the reflection marks may move slightly and/or change their orientation on the surface of the test bars. For this reason, the measured strains were referred to as the strains $\epsilon_{\text{TT}}(\sigma_0)$ determined by tensile tests that occurred for the given initial stresses σ_0. Therefore the measured strains were corrected as follows:

$$\Delta\varepsilon = \varepsilon_{\text{TT}}(\sigma_0) - \varepsilon_0 \tag{9}$$

with strain correction $\Delta\epsilon$.

2.2.4 Data evaluation of creep curves

The creep curves were evaluated in the following way:

- Correction of the measured strains with $\Delta\epsilon$, equation (9)
- Conversion to the measured creep compliance $J_{\text{meas}}(t, \sigma_0)$ – division of strains $\epsilon(t)$ by the initial stresses σ_0
- Determination of the ultimate creep compliances $J_{\text{ultimate}}(t, \sigma_0)$
- Determination of the calculated creep compliances taking into account the FOD
- Comparison of measured and calculated creep compliances

The comparison allows for determining the range of correspondence of the matrix and composite creep, which depends on the creep time and initial stresses.

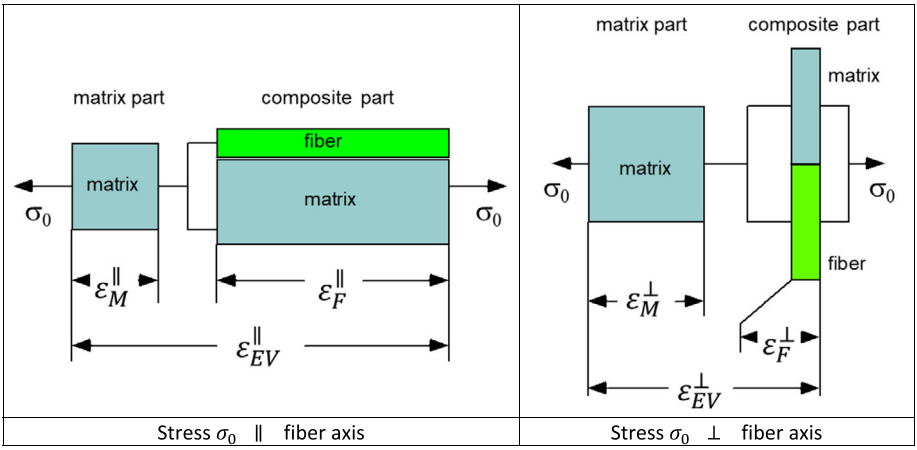

Fig. 3 Scheme for dividing the EV into *matrix* and *composite* parts with stresses acting parallelly and perpendicularly to the fiber axis (Color figure online)

2.2.5 Morphological investigations

Fracture surfaces parallel and perpendicular to the flow direction of both the CIM and PPP test bars were sputtered with gold (Emscope SC 500). Subsequent investigation using a scanning electron microscope (Jeol JSM 6300 F) with an acceleration voltage of 20 kV provided qualitative information on the fiber-matrix adhesion and deformation mechanisms.

3 Theoretical considerations

3.1 Derivation of time-dependent compliances of SFRC

If an EV (Fig. 3) is loaded by a constant stress σ_0, then it starts to creep and exhibits a time-dependent increase in strain $\varepsilon_{\mathrm{EV}}(t)$. It is clear that the "macroscopic" strain $\varepsilon_{\mathrm{EV}}(t)$ differs from the strains of the matrix part $\varepsilon_{\mathrm{M}}(t)$ and the composite part $\varepsilon_{\mathrm{F}}(t)$. These strains depend on the orientation of the fibers with respect to the direction of σ_0. Therefore it is necessary to calculate the strains parallel to the fiber axis $\varepsilon_{\mathrm{EV}}^{\parallel}(t)$ and perpendicular to the fiber axis $\varepsilon_{\mathrm{EV}}^{\perp}(t)$ by dividing EV, as shown in Fig. 3.

3.2 Case 1: stress σ_0 acts parallelly to fiber axis

The initial stress σ_0 strains the EV to

$$\varepsilon_{\mathrm{EV}}^{\parallel} = \frac{\Delta\,(L+a)}{(L+a)} = \frac{\Delta L}{(L+a)} + \frac{\Delta a}{(L+a)} = \frac{L}{(L+a)}\underbrace{\frac{\Delta L}{L}}_{=\varepsilon_{\mathrm{F}}^{\parallel}} + \frac{a}{(L+a)}\underbrace{\frac{\Delta a}{a}}_{=\varepsilon_{\mathrm{M}}^{\parallel}}. \tag{10}$$

Extending denominator and nominator with the fiber diameter D yields

$$\varepsilon_{\mathrm{EV}}^{\parallel} = \frac{r}{(r+d)}\varepsilon_{\mathrm{F}}^{\parallel} + \frac{d}{(r+d)}\varepsilon_{\mathrm{M}}^{\parallel} \tag{11}$$

with aspect ratio r and normalized fiber distance d given by

$$d = d\left(v_{\mathrm{F}}, r\right) = \frac{a}{D}. \tag{12}$$

3.3 Case 2: stress σ_0 acts perpendicularly to fiber axis

The initial stress σ_0 strains the EV to

$$\varepsilon_{\mathrm{EV}}^{\perp} = \frac{\Delta\left(D+a\right)}{\left(D+a\right)}. \tag{13}$$

Because the fiber has a circular cross-section, the reference lengths of the matrix and composite parts must be corrected using the geometry constant k:

$$\begin{aligned}\varepsilon_{\mathrm{EV}}^{\perp} &= \frac{\Delta k D}{\left(D+a\right)} + \frac{\Delta a + \Delta\left(1-k\right)D}{\left(L+a\right)} \\ &= \frac{kD}{\left(D+a\right)} \underbrace{\frac{\Delta L}{kD}}_{=\varepsilon_{\mathrm{F}}^{\perp}} + \frac{a+\left(1-k\right)D}{\left(D+a\right)} \underbrace{\frac{\Delta a}{a+\left(1-k\right)D}}_{=\varepsilon_{\mathrm{M}}^{\perp}}.\end{aligned} \tag{14}$$

The geometric constant k depends on the inclusion shape. For short fibers, it can be determined by conversion to a square column-shaped fiber with the same length L and cross-section A:

$$A_{\text{fiber}} = \frac{\pi}{4}D^2 = A_{\text{square column}} = k^2 D^2 \quad \Rightarrow \quad k = \sqrt{\frac{\pi}{4}} \cong 0.886. \tag{15}$$

Extending denominator and nominator with the fiber diameter D yields

$$\varepsilon_{\mathrm{EV}}^{\perp} = \frac{k}{\left(1+d\right)}\varepsilon_{\mathrm{F}}^{\perp} + \frac{d+1-k}{\left(1+d\right)}\varepsilon_{\mathrm{M}}^{\perp}. \tag{16}$$

Equations (10) and (15) link the *macroscopic strain* of the EV to *microscopic strains* of both the matrix and composite parts with weighting factors depending only on the geometry of the EV. In the general case of a creep experiment, all strains in equations (11) and (16) depend on time and stress. Dividing these strains by the initial stress σ_0 yields the time- and stress-dependent creep compliance parallel to the fiber axis,

$$J_{\mathrm{EV}}^{\parallel}\left(t, \sigma_0\right) = \frac{r}{\left(r+d\right)}J_{\mathrm{F}}^{\parallel}\left(t, \sigma_0\right) + \frac{d}{\left(r+d\right)}J_{\mathrm{M}}^{\parallel}\left(t, \sigma_0\right), \tag{17}$$

and perpendicular to the fiber axis,

$$J_{\mathrm{EV}}^{\perp}\left(t, \sigma_0\right) = \frac{k}{\left(1+d\right)}J_{\mathrm{F}}^{\perp}\left(t, \sigma_0\right) + \frac{d+1-k}{\left(1+d\right)}J_{\mathrm{M}}^{\perp}\left(t, \sigma_0\right). \tag{18}$$

If the initial stress σ_0 remains small compared with the yield stress $\sigma_{y,}$ then we can assume that the composite part behaves purely elastically. This means that the creep compliances $J_{\mathrm{F}}^{\parallel}\left(t,\ \sigma_0\right)$ and $J_{\mathrm{F}}^{\perp}\left(t,\ \sigma_0\right)$ remain constant and can be substituted by the corresponding compliances at $t = 0$ given by the reciprocal moduli of the composite part. Furthermore, the

chosen temperatures at which creep experiments are performed strongly affect the creep behavior. As equation (16) holds for any temperature T, it is introduced in equations (19) and (20). This leads to

$$J_{\mathrm{EV}}^{\parallel}(t,\sigma_0,T) = \frac{r}{(r+d)} \underbrace{\frac{1}{E_{\mathrm{F}}A_{\mathrm{F}}^{\parallel} + E_{\mathrm{M}}\left(1-A_{\mathrm{F}}^{\parallel}\right)}}_{=\frac{1}{E_{composite part}^{\parallel}}} + \frac{d}{(r+d)} J_{\mathrm{M}}^{\parallel}(t,\sigma_0,T) \quad \text{with } A_{\mathrm{F}}^{\parallel} = \frac{\frac{\pi}{4}}{(1+d)^2} \tag{19}$$

and

$$J_{\mathrm{EV}}^{\perp}(t,\sigma_0,T) = \frac{k}{(1+d)} \underbrace{\frac{1}{E_{\mathrm{F}}A_{\mathrm{F}}^{\perp} + E_{\mathrm{M}}\left(1-A_{\mathrm{F}}^{\perp}\right)}}_{=\frac{1}{E_{composite part}^{\perp}}} + \frac{d+1-k}{(1+d)} J_{\mathrm{M}}^{\perp}(t,\sigma_0,T) \quad \text{with } A_{\mathrm{F}}^{\perp} = \frac{kr}{(r+d)(1+d)} \tag{20}$$

with fiber modulus E_{F}, matrix modulus E_{M}, and relative cross-sections of the fiber parallel to the fiber axis $A_{\mathrm{F}}^{\parallel}$ and perpendicular to the fiber axis $A_{\mathrm{F}}^{\perp}$. From equations (19) and (20) we can conclude that the creep compliance of SFRC is completely determined by the creep compliances of the matrix as long as the initial stresses remain small compared to the yield stresses. Thus the ultimate creep compliances of SFRC with known fiber volume content and aspect ratio can be calculated only by the measured creep compliances of the matrix at given initial stresses and temperatures. However, we have to keep in mind that close to glass transition temperature, matrix properties depend strongly on time and initial stress. This means that E_{M} in the composite part becomes time dependent. Therefore modeling should not be performed at temperatures $T_{\mathrm{G}} \pm 15$ K. (In the following text the temperature T is not explicitly shown in the formulas.)

3.3.1 Calculation of the creep compliances taking into account fiber orientation

The orientation factor f_3 in the thickness direction was close to zero for all composites. This means that the plates are close to the lamina, and the fiber orientation can be considered according to Jones (1975) for the plane stress state. The stress–strain relation of the transversely isotropic EV in the main axis system is given by

$$\begin{pmatrix}\varepsilon_1\\ \varepsilon_2\\ \varepsilon_3\end{pmatrix} = \begin{pmatrix}\varepsilon_1\\ \varepsilon_2\\ \gamma_{12}\end{pmatrix} = \begin{pmatrix}J_{11} & J_{12} & 0\\ J_{12} & J_{22} & 0\\ 0 & 0 & J_{66}\end{pmatrix}\begin{pmatrix}\sigma_1\\ \sigma_2\\ \tau_{12}\end{pmatrix} \tag{21}$$

with

$$J_{11} = \frac{1}{E_{11}}, \quad J_{12} = -\frac{\nu_{12}}{E_{11}} = -\frac{\nu_{21}}{E_{22}}, \quad J_{22} = \frac{1}{E_{22}}, \quad \text{and} \quad J_{66} = \frac{1}{G_{12}}. \tag{22}$$

Usually, the coordinate system of a part differs from the main axis system of the EV, requiring a transformation leading to

$$\begin{pmatrix} \varepsilon_x \\ \varepsilon_y \\ \varepsilon_z \end{pmatrix} = \begin{pmatrix} \varepsilon_x \\ \varepsilon_y \\ \gamma_{xy} \end{pmatrix} = \begin{pmatrix} \overline{J}_{11} & \overline{J}_{12} & \overline{J}_{16} \\ \overline{J}_{12} & \overline{J}_{22} & \overline{J}_{26} \\ \overline{J}_{16} & \overline{J}_{26} & \overline{J}_{66} \end{pmatrix} \begin{pmatrix} \sigma_x \\ \sigma_y \\ \tau_{xy} \end{pmatrix}. \tag{23}$$

The components of the $\bar{J}$-matrix depend on the components of the J-matrix and the angle θ of misalignment of the fiber orientation to the direction of the external load:

$$\bar{J}_{11} = J_{11}\cos^4\theta + (2J_{12} + J_{66})\sin^2\theta\cos^2\theta + J_{22}\sin^4\theta, \tag{24a}$$

$$\bar{J}_{12} = J_{12}\left(\sin^4\theta + \cos^4\theta\right) + (J_{11} + J_{22} - J_{66})\sin^2\theta\cos^2\theta, \tag{24b}$$

$$\bar{J}_{22} = J_{11}\sin^4\theta + (2J_{12} + J_{66})\sin^2\theta cos^2\theta + J_{22}\cos^4\theta, \tag{24c}$$

$$\bar{J}_{16} = (2J_{11} - 2J_{12} - J_{66})\sin\theta\cos^3\theta - (2J_{22} - 2J_{12} - J_{66})\sin^3\theta\cos\theta, \tag{24d}$$

$$\bar{J}_{26} = (2J_{11} - 2J_{12} - J_{66})\sin^3\theta\cos\theta - (2J_{22} - 2J_{12} - J_{66})\sin\theta\cos^3\theta, \tag{24e}$$

$$\bar{J}_{66} = 2\,(2J_{11} + 2J_{22} - 4J_{12} - J_{66})\sin^2\theta\cos^2\theta + J_{66}\left(\sin^4\theta + \cos^4\theta\right), \tag{24f}$$

where J_{ij} are defined in terms of the engineering constants in Eq. (22). To measure the creep parallel to the flow direction, the stress $\sigma_0 = (\sigma_0, 0, 0)$ must be applied in the x-direction, leading to

$$\begin{aligned} \overline{J}_{11}(t, \sigma_0) &= \frac{1}{E_{11}}\cos^4\theta + \left(-\frac{2\nu_{12}}{E_{11}} + \frac{1}{G_{12}}\right)\sin^2\theta\cos^2\theta + \frac{1}{E_{22}}\sin^4\theta \\ &= J_{11}(t, \sigma_o)\cos^4\theta + \left(-2\nu_{12}J_{11}(t, \sigma_o) + \frac{1}{G_{12}(t, \sigma_0)}\right)\sin^2\theta\cos^2\theta \\ &\quad + J_{22}(t, \sigma_o)\sin^4\theta, \end{aligned} \tag{25}$$

and to measure the creep perpendicular to the flow direction, the stress $\sigma_0 = (0, \sigma_0, 0)$ has to be applied in the y-direction, leading to

$$\begin{aligned} \overline{J}_{22}(t, \sigma_0) &= \frac{1}{E_{11}}\sin^4\theta + \left(-\frac{2\nu_{12}}{E_{11}} + \frac{1}{G_{12}}\right)\sin^2\theta\cos^2\theta + \frac{1}{E_{22}}\cos^4\theta \\ &= J_{11}(t, \sigma_o)\sin^4\theta + \left(-2\nu_{12}J_{11}(t, \sigma_o) + \frac{1}{G_{12}(t, \sigma_0)}\right)\sin^2\theta\cos^2\theta \\ &\quad + J_{22}(t, \sigma_o)\cos^4\theta. \end{aligned} \tag{26}$$

Equations (25) and (26) contain the shear modulus G_{12}, which was not evaluated experimentally. Consequently, it must be determined or approximated differently. The EVC formally provides identical terms for E_{22} and G_{12} (Appendix A). As the PBT matrix and glass fibers can be considered isotropic materials, the corresponding shear moduli can be expressed by their Young moduli and Poisson ratios:

$$G_M = \frac{E_M}{2\,(1 + \nu_M)} \quad \text{or} \quad G_F = \frac{E_F}{2\,(1 + \nu_F)}. \tag{27}$$

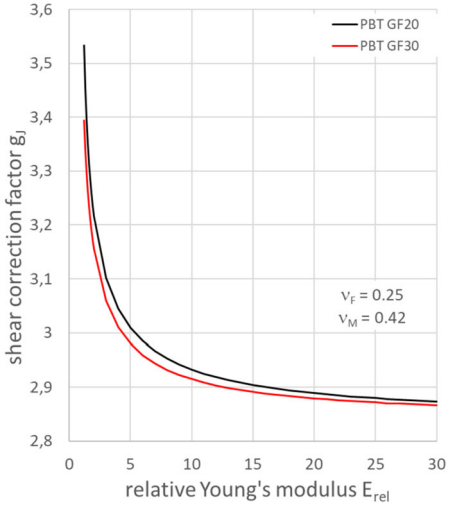

Fig. 4 Dependence of relative modulus E_{rel} of fiber and matrix on shear correction factor g_J (Color figure online)

The introduction of equation (27) into the EVC term for G_{12} in Appendix A and rearranging the right-hand side leads to

$$\frac{1}{G_{12}(t,\sigma_0)} = J_{22}(t,\sigma_0)\,\underbrace{2(1+\nu_M)\left[\frac{1+\frac{(1+d-k)\frac{(\nu_M-\nu_F)}{(1+\nu_F)}E_R+(1+d-k)\frac{(\nu_M-\nu_F)}{(1+\nu_F)}A_F^{\perp}E_R}{k+(1+d-k)(E_R-1)+(1+d-k)A_F^{\perp}(E_R-1)}}{1+\frac{\frac{(\nu_M-\nu_F)}{(1+\nu_F)}A_F^{\perp}E_R}{1+A_F^{\perp}(E_R-1)}}\right]}_{\text{shear correction factor } g_J}. \tag{28}$$

The shear correction factor g_J depends firstly on the material properties, *relative modulus* and *Poisson's ratios* of the fiber and matrix, and secondly, on the geometry of the EV given by *aspect ratio* r and *normalized fiber distance* d. Short fiber-reinforced PBT composites consist of fibers with aspect ratios between 20 and 40, meaning that the normalized fiber distance remains almost constant. The Poisson ratio ν of PBT is 0.42, and the Poisson ratios of the glass fibers range from 0.18 to 0.30 Kojima (2024). Their effects on the relative modulus E_{rel} are shown in Fig. 4 for the Poisson ratio $\nu_F = 0.25$. If the relative moduli exceed 10, injection-molded short glass fiber-reinforced composites have relative moduli of typically 15 to 40, the shear correction factor g_J decreases from 2.95 to 2.85 for both PBT GF20 and PBT GF30. If the Poisson ratio increases from 0 to 0.5, then the shear correction factor g_J decreases from 2.93 to 2.82, Fig. 5.

For relative moduli exceeding 30, the shear correction factor g_J asymptotically approaches 2.8. Thus, for both the PBT GF20 and PBT GF30 composites, a shear correction factor of 2.85 is a good estimate. Due to the relaxation processes, the matrix moduli decreased during the creep experiment; however, this did not significantly affect the shear correction factor g_J. The key consequence is that the time and stress dependency of $J_{66} = \frac{1}{G_{12}}$ corresponds directly to the time and stress dependency of J_{22}:

$$J_{66} = J_{22} g_J. \tag{29}$$

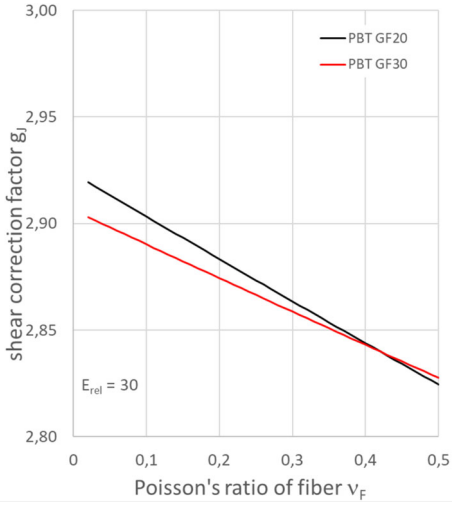

Fig. 5 Dependence of Poisson's ratio of fibers on shear correction factor g_J (Color figure online)

Table 3 Effects of processing – conventional injection molding (CIM) or push–pull processing (PPP), respectively. On mean fiber length or aspect ratio and orientation factors, fiber diameter is 7 µm according to the manufacturer

Material	Processing	Mean fiber length $\langle L \rangle$ µm	Aspect ratio r	Orientation factors		
				$f_1 = \cos^2\theta$	f_2	f_3
PBT GF20	granules	255	36	-	-	-
PBT GF20	PPP	212	30	0.753	0.211	0.036
PBT GF20	CIM	235	34	0.713	0.253	0.034
PBT GF30	granules	288	41	-	-	-
PBT GF30	PPP	199	28	0.800	0.173	0.027
PBT GF30	CIM	200	28	0.705	0.261	0.034

3.4 Results and discussion

3.4.1 Experimental results

To determine the creep compliances parallel and perpendicular to the fiber axis of the EV according to equations (19) and (20), the mean aspect ratio r has to be measured, which determines the normalized fiber distance together with the fiber volume content, Table 3. We can see that injection molding causes fiber length degradation on the order of 20 to 30%, which is more pronounced for PPP (push–pull processing) and higher fiber contents. Furthermore, as the plates are not uniaxially oriented SFRC, the fiber orientation had to be determined, Table 3. As expected, the plates have a preferential fiber orientation, with orientation factors being higher for PPP than for conventional injection molding (CIM). The orientation factors in the thickness direction f_3 are close to 0, justifying the laminate evaluation.

The mechanical properties (Table 4) show that PPP leads to slightly larger Young's moduli and yield stresses for neat PBT, which was also reported for PP (Kech et al. 2000). For

Table 4 Young's moduli, tensile strengths, and elongations at break of PBT composites determined by tensile tests according to ISO 527, with standard deviations (STD) and Young's moduli for calculating compliance predictions

	Young's modulus MPa mean STD	Yield stress MPa mean STD	Yield strain % mean STD	Young's modulus for calculation MPa
PBT matrix				
CIM ∥	2385 ± 64	52.6 ± 1.0	3.00 ± 0.01	2400
CIM ⊥	2417 ± 10	53.3 ± 0.1	3.02 ± 0.02	
PPP ∥	2524 ± 45	54.5 ± 0.4	3.05 ± 0.20	2500
PPP ⊥	2492 ± 54	54.6 ± 0.1	3.07 ± 0.05	
PBT GF20				
CIM ∥	5498 ± 211	100.0 ± 3.8	3.05 ± 0.19	5500
CIM ⊥	3882 ± 108	69.3 ± 1.3	3.88 ± 0.10	3900
PPP ∥	6207 ± 273	105.0 ± 1.9	2.66 ± 0.16	6200
PPP ⊥	3642 ± 140	50.8 ± 1.1	1.90 ± 0.11	3650
PBT GF30				
CIM ∥	7400 ± 373	115.8 ± 0.8	2.52 ± 0.40	7400
CIM ⊥	4427 ± 111	68.4 ± 1.8	3.77 ± 0.06	4400
PPP ∥	8692 ± 103	101.0 ± 5.6	1.51 ± 0.11	8700
PPP ⊥	4308 ± 315	46.2 ± 1.8	1.31 ± 0.04	4300

PBT GF20 and PBT GF30, the Young moduli parallel to the flow direction were 50% higher for CIM and 80% higher for PPP compared to those perpendicular to the flow direction. For the CIM, the yield stresses behave similarly, whereas the yield stresses parallel to the flow direction are 100% higher for PPP. Furthermore, the yield stresses perpendicular to the flow direction of the PPP test bars did not exceed the yield stresses of neat PBT. The highly oriented PPP samples fractured at an elongation at break of approximately 50% compared with the less oriented CIM samples. The Young moduli in Table 4 were also used to correct the creep strains according to equation (9).

The creep compliances of neat PBT start at 0.42 GPa^{-1} for CIM and 0.38 GPa^{-1} for PPP, independently of the initial stresses. This corresponds to different matrix stiffnesses due to the processing method. However, the creep compliances increase faster with time as the initial stresses increase and exhibit a pronounced time and stress dependency. The splitting of the creep compliance curves of neat PBT and PBT GF (glass fiber filled) indicates that the nonlinear creep behavior is pronounced at an initial stress of 37.5 MPa.

The introduction of glass fibers reduced the initial creep compliances of PBT GF20 by approximately 60–65% perpendicular to the flow direction and 40–50% parallel to the flow direction, and of PBT GF30 by approximately 50–60% perpendicular to the flow direction and 30–35% parallel to the flow direction, Fig. 6. Furthermore, the creep rates decreased with increasing GF content.

The CIM samples exhibit a linear viscoelastic behavior, indicated by the coinciding creep compliance curves, up to initial stresses of 25 MPa perpendicular to the flow direction and up to 37.5 MPa parallel to the flow direction. PPP samples of PBT GF 20 did not behave linear viscoelastically perpendicular to the flow direction and exhibited more creep than the CIM samples, and at 37.5 MPa, fracture occurred after one day. The corresponding PBT GF30

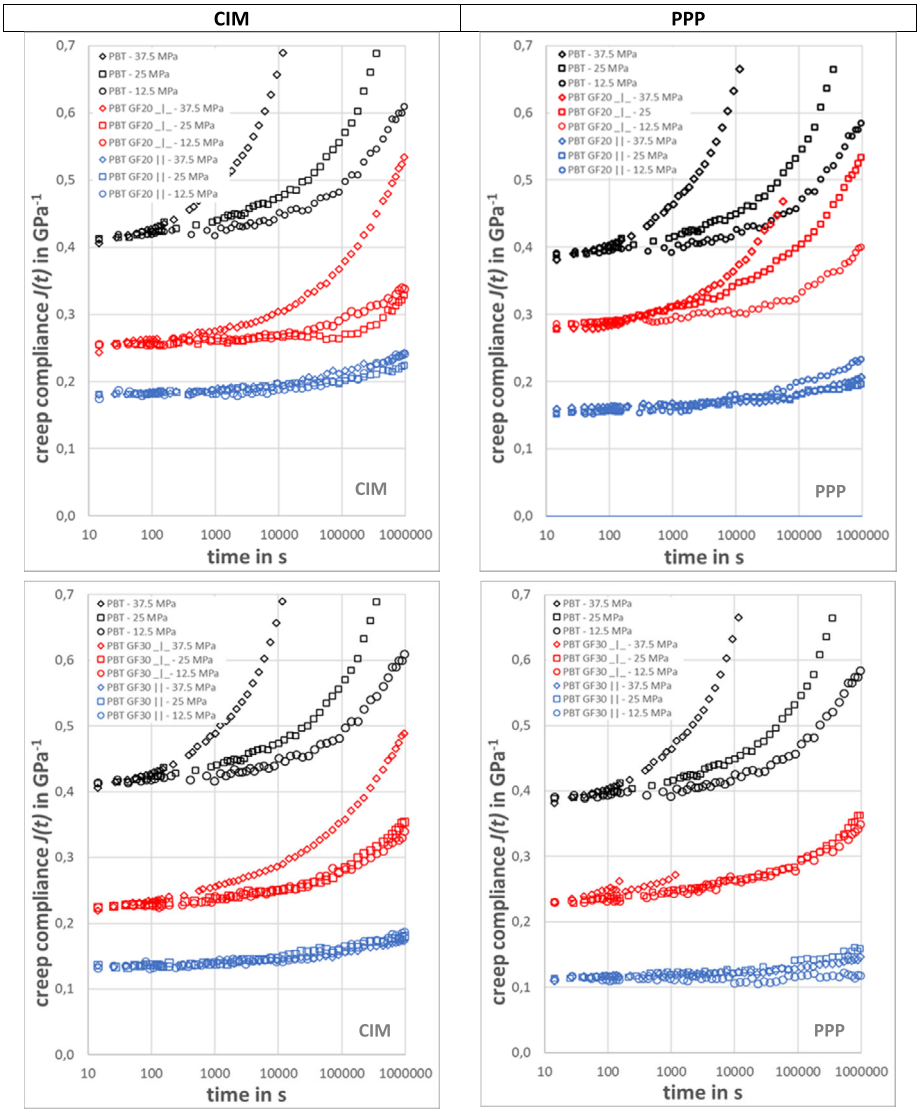

Fig. 6 Creep compliances parallel and perpendicular to the flow direction of neat PBT, PBT GF20 (top), and PBT GF30 (bottom) processed by CIM (left) and PPP (right) for initial stresses of 12.5 MPa (o), 25 MPa (□), and 37.5 MPa (◊) (Color figure online)

samples exhibit linear viscoelastic behavior up to initial stresses of 25 MPa but fracture after 2 to 20 minutes at 37.5 MPa. This indicates that the matrix deformability decreases with the GF content for stresses close to the yield stress of the matrix. Parallel to the flow direction, the creep compliances of both PBT GF20 and PBT GF30 coincided for all initial stresses within the experimental error, indicating linear viscoelastic behavior up to at least 37.5 MPa. In general, we can say that PPP increases creep compliance perpendicular to the flow direction and reduces it parallel to it.

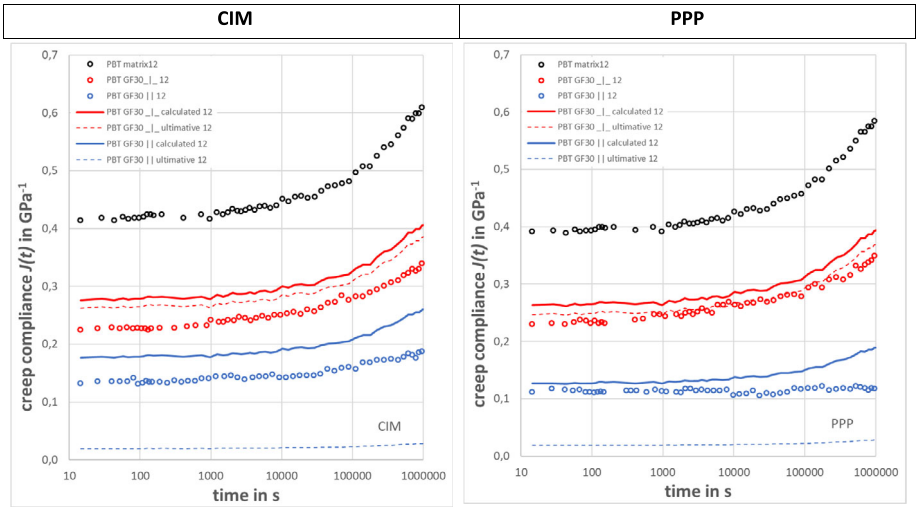

Fig. 7 Comparison of measured creep compliances (symbols) of PBT GF30 processed by CIM (left) and PPP (right) to calculated creep compliances according to equations (25), (26), and (29) (solid lines) and ultimate creep compliances (dashed lines); $\perp$ data in red, $\parallel$ data in blue, $\sigma_0 = 12.5$ MPa (Color figure online)

3.5 Calculation of predicted creep compliances and comparison to measurements

First, the predictions of the creep compliances were calculated using equations (19) and (20) in combination with equation (21). The required input data were obtained from Tables 3 and 4. The Poisson ratios ν_{12} were calculated to be 0.0044 (PBT GF20) and 0.0061 (PBT GF30), which are both close to *zero*. These small Poisson's ratios result from the highly oriented long fibers, which prevent most of the contraction in the fiber direction.

A comparison of the measured and calculated creep compliances is shown for PBT GF30 for an initial stress of 12.5 MPa in Fig. 7. The predicted time dependency of the creep compliances was reproduced quite well, and the predictions had a stress-dependent time limit due to the start of the pronounced creep of the PBT matrix. Evidently, the fibers affect the creep mechanisms. The predictions overestimate the creep compliances of PPP samples by 20% and CIM samples by 40% in the $\parallel$-direction and 30% in the $\perp$-direction. This could be partly explained by the fact that PBT GF may have higher crystallinities due to the nucleation effects of the fibers and differences in processing such as higher melt temperatures because of more internal friction due to the fibers leading to longer solidification times. Möginger (1992) investigated the effects of processing in terms of the melt temperature, mold temperature, and cycle time on the properties of neat PBT. He found increasing crystallinities with melt temperatures from 30% to 36%, which led to variations in the PBT creep compliances of up to 100%. From this perspective the predictions can be considered fairly good.

However, a crucial flaw exists in these predictions: the predicted creep compliances perpendicular to the flow direction always exceed the ultimate creep compliances, and the ultimate creep compliances represent the upper bounds. Equations (24a)–(24f) represent the creep compliances of unidirectional continuous fiber-reinforced composites in which the fibers are misaligned by the angle θ to the direction of the external stress. An analysis shows that the substitution of J_{66} by J_{22} using equation (29) significantly increases the creep strain contribution of the shear term. J_{22} was determined under normal stress, and J_{66} under shear

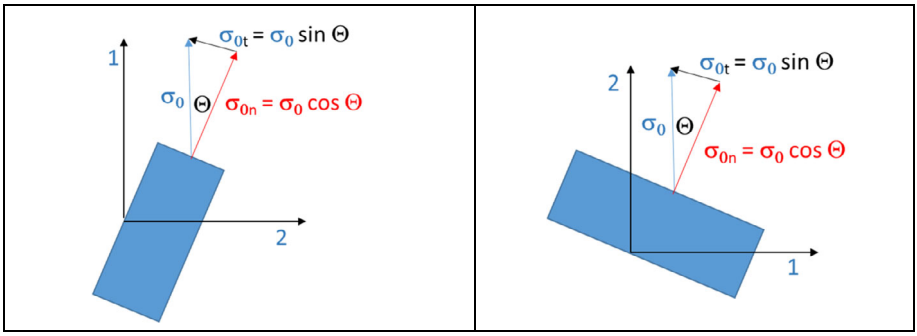

Fig. 8 Determination of effective stresses due to a fiber misalignment θ (Color figure online)

stress. Thus further correction is required considering that the creep-inducing shear stresses are smaller than the applied tensile stresses, thus reducing the predicted creep compliances.

In creep experiments, deformations were measured parallel and perpendicular to the flow direction and converted to creep strains. From Fig. 8 it becomes evident that G_{12} is not determined by the initial stress s0 but by the smaller shear stress σ_{0t} given by

$$\sigma_{0t} = \sigma_0 \sin\theta. \tag{30}$$

This leads to the following modification of the shear correction factor g_J from Eq. (28):

$$G_J = g_J \sin\theta \tag{31}$$

with the effective shear correction factor G_J. Considering this, the calculated creep compliance $\bar{J}_{11}(t, \sigma_0)$ parallel to the flow direction changes to

$$\begin{aligned}\overline{J}_{11}(t,\sigma_0) &= J_{11}(t,\sigma_0)\, cos^4\theta - 2\nu_{12} J_{11}(t,\sigma_0)\sin^2\theta\cos^2\theta \\ &\quad + g_J J_{22}(t,\sigma_0)\sin^3\theta\cos^2\theta + J_{22}(t,\sigma_0)\sin^4\theta \\ &= J_{11}(t,\sigma_0)\, cos^4\theta - 2\nu_{12} J_{11}(t,\sigma_0)\sin^2\theta\cos^2\theta \\ &\quad + G_J J_{22}(t,\sigma_0)\sin^2\theta\cos^2\theta + J_{22}(t,\sigma_0)\sin^4\theta,\end{aligned} \tag{32}$$

and the measured creep compliance $\bar{J}_{22}(t, \sigma_0)$ perpendicular to the flow direction to

$$\begin{aligned}\overline{J}_{11}(t,\sigma_0) &= J_{11}(t,\sigma_0)\, sin^4\theta - 2\nu_{12} J_{11}(t,\sigma_0)\sin^2\theta\cos^2\theta \\ &\quad + g_J J_{22}(t,\sigma_0)\sin^3\theta\cos^2\theta + J_{22}(t,\sigma_0)\sin^4\theta \\ &= J_{11}(t,\sigma_0)\, sin^4\theta - 2\nu_{12} J_{11}(t,\sigma_0)\sin^2\theta\cos^2\theta \\ &\quad + G_J J_{22}(t,\sigma_0)\sin^2\theta\cos^2\theta + J_{22}(t,\sigma_0)\sin^4\theta.\end{aligned} \tag{33}$$

The creep compliance calculated according to equations (32) and (33) are compared to measured creep compliances of PBT GF20 (Fig. 9) for $\sigma_0 = 12.5$ MPa and (Appendix B) for $\sigma_0 = 25$ MPa and 37.5 MPa, and PBT GF30 (Fig. 10) for $\sigma_0 = 12.5$ MPa and (Appendix C (for $\sigma_0 = 25$ MPa and 37.5 MPa. Now the ultimate creep compliance perpendicular to the

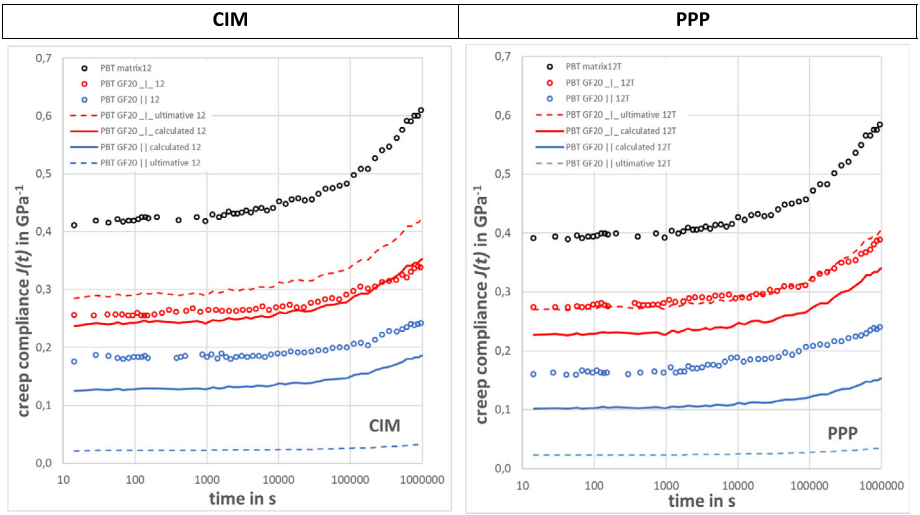

Fig. 9 Comparison of measured creep compliances (symbols) of PBT GF20 processed by CIM (left) and PPP (right) to calculated creep compliances (solid lines) and ultimate creep compliances (dashed lines); $\perp$ data in red, $\parallel$ data in blue, $\sigma_0 = 12.5$ MPa (Color figure online)

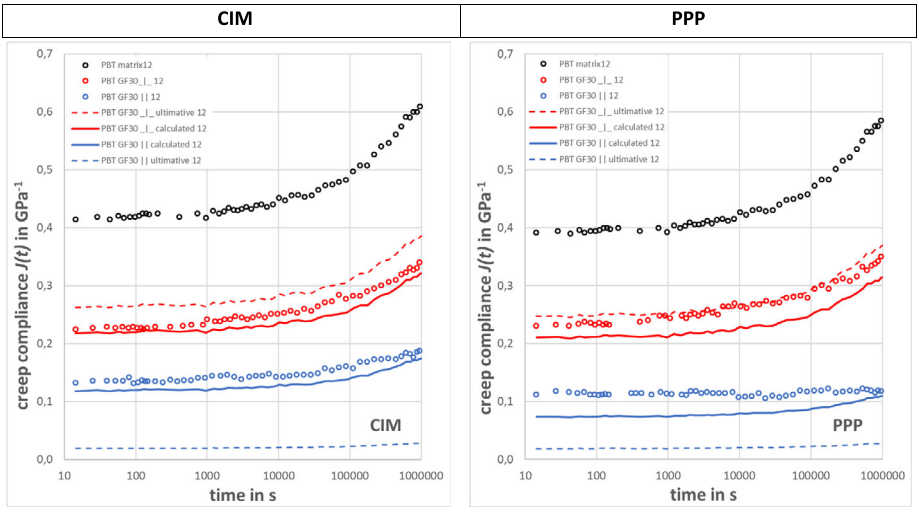

Fig. 10 Comparison of measured creep compliances (symbols) of PBT GF30 processed by CIM (left) and PPP (right) to calculated creep compliances (solid lines) and ultimate creep compliances (dashed lines); $\perp$ data in red, $\parallel$ data in blue, $\sigma_0 = 12.5$ MPa (Color figure online)

flow direction exceeded the corresponding measured creep compliance, and the measured creep compliance always exceeded the predictions. In principle, this is good news, as the assumptions *perfect fiber matrix adhesion* and *purely elastic behavior of the composite part* should provide calculated creep compliances smaller than the measured ones. Furthermore, the time range of proper modeling is decreased with initial stress and characterized by a

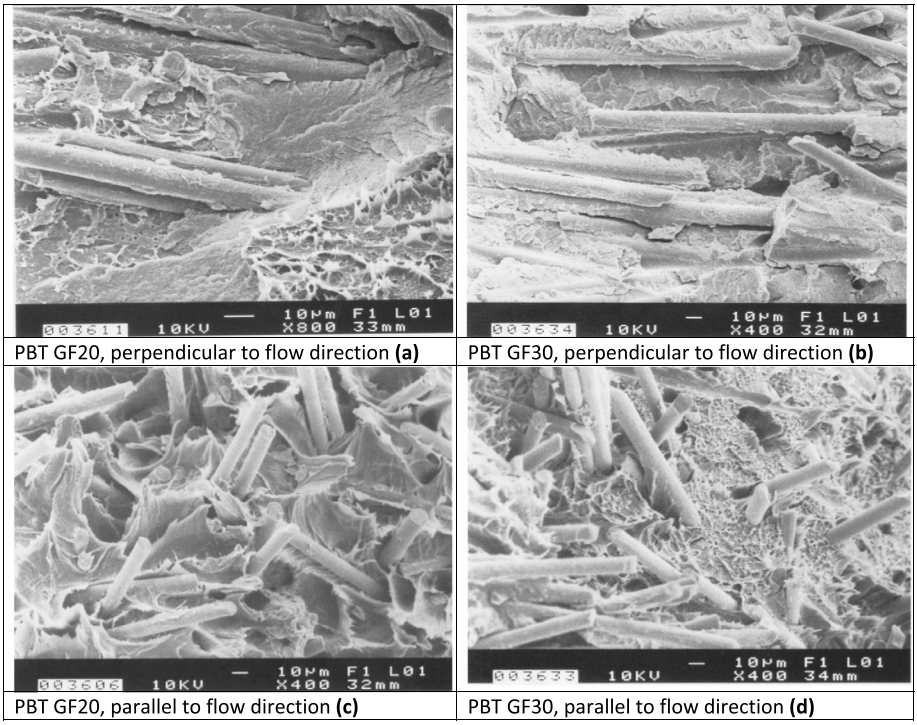

Fig. 11 SEM pictures of fracture surfaces of PBT GF

specific time limit. The reason for this behavior is that the creep of the neat matrix starts to propagate if the specific time limit is exceeded.

3.6 SEM investigation of fracture surfaces parallel and perpendicular to the flow direction

The SEM images of the fracture surfaces (Fig. 11) show that the matrix material adhered to the fiber surfaces to a relatively large extent, indicating good fiber-matrix adhesion. This behavior was more pronounced for fibers oriented perpendicularly to the stress direction, where the interface was subjected to tensile stress. In the case of good fiber-matrix adhesion, the tensile interface strength exceeds the shear strength of the matrix. As the tensile stress approached the shear strength, the matrix still adhered well to the fibers, but started to exhibit shear flow failure in the vicinity of the fibers. If fracturing occurs, a zigzag-shaped matrix structure on the fiber surface is generated due to shear flow at 45°, Figs. 11 a and b. If the fibers are oriented parallelly to the stress direction, then the external tensile stress is transferred by shear stresses along the interface to the fibers. Due to this stress transfer mechanism, the end regions of the fibers were subjected to a constant maximum shear stress. If this shear stress corresponds to the shear strength of the matrix, then the matrix slides along the fiber surface, leading to fiber pullout and delamination. Consequently, the end regions of the fibers oriented parallelly to the stress exhibit hardly any matrix adherences, Figs. 11 c and d. The matrix adherences are mainly visible on the fibers that are significantly oriented perpendicularly to the stress direction. Thus the SEM images of the fracture surfaces show

that the fiber-matrix adhesion is good but not perfect and that it seems to depend on the stress direction at the interface.

Rech et al. (2022a) introduced an adhesion factor k_{adh} to account for the effects of varying the fiber-matrix adhesions in glass bead-reinforced thermoplastics. A smaller adhesion factor increased the elastic compliance of the composite part of the EV. From creep experiments of glass bead-reinforced PBT the short-term adhesion factor was determined as $k_{\text{adh}} \approx 0.5$ ($t < 1{,}000$ s), and the long-term adhesion factor as $k_{\text{adh}} \approx 0.3$ ($t > 100{,}000$ s), far from the perfect case $k_{\text{adh}} \approx 1$ (Rech et al. 2022b). The fracture and failure behaviors shown in Fig. 11 suggest that the adhesion factor k_{adh} depends either on the angle θ between the initial stress and main fiber orientation or that we have to distinguish two adhesion factors attributed to tensile or shear failure.

With increasing initial stress σ_0, the time range decreases significantly, in which the time dependency of the matrix creep corresponds to the creep of SFRC (Appendices B and C). To evaluate this *creep time limit* t_{limit}, the relative deviations of the measured creep compliances from the calculated ones are required:

$$\Delta J_{rel}(t) = \frac{J_{meas}(t) - J_{calc}(t)}{J_{meas}(t)}. \tag{34}$$

Creep compliances were determined to be parallel ($\parallel$) and perpendicular ($\perp$) to the flow direction. The creep time limit was assumed to be achieved if $\Delta J_{rel}(t)$ became smaller than 80% of $\Delta J_{rel}(t = 0)$,

$$\Delta J_{rel}(t = t_{\text{limit}}) = 0.8 \Delta J_{rel}(t = 0). \tag{35}$$

The evaluation shows that t_{limit} decreases by a factor of approximately 30 with each increase in the initial stress, Table 5. It also appears that t_{limit} is achieved at shorter times if the stress acts perpendicularly to the flow direction. Furthermore, we can see that $\Delta J_{\text{rel},\parallel}$ exceeds $\Delta J_{\text{rel},\perp}$ a factor of 2 to 4. This indicates that the *composite part of the EV* must exhibit some shear creep of its matrix not yet taken into account by the modeling.

Plotting the creep time limits t_{limit} in Table 5 versus the initial stresses σ_0 reveals a logarithmic dependency with reasonable correlation coefficients (Table 6):

$$\sigma_{0,i} = a_1 \lg \frac{t_{\text{limit},i}}{t_0} + a_0 \tag{36}$$

with reference time t_0 (e.g., 1 s), fit parameter slope a_1, and interception a_0.

The interceptions correspond well to the yield strengths σ_{yield} of PBT (Table 4) and exhibit a standard deviation (STD) of typically 3 MPa. The mean slopes $a_{1,\parallel}$ and $a_{1,\perp}$ were determined to be (-7.8 ± 0.64) MPa ($\parallel$) and (-7.6 ± 0.15) MPa ($\perp$), respectively. The STD of the slopes $a_{1,\parallel}$ are four times larger than the slopes $a_{1,\perp}$. This may indicate that cross-sectional variations in fiber orientation affect the creep behavior parallel to the flow direction in a more pronounced manner. Solving Equation (36) with respect to the *creep time limit* yields an exponential decrease with the initial stress:e

$$t_{\text{limit},i} = t_0 * 10^{-\frac{a_0 - \sigma_{0,i}}{a_1}} \cong t_0 * 10^{-\frac{\sigma_{\text{yield}} - \sigma_{0,i}}{a_1}}. \tag{37}$$

From equation (37) it follows that the creep behavior of SFRC PBT can be predicted by the matrix creep with sufficient accuracy if the initial load does not exceed 12.5 MPa ($\approx \sigma_{\text{yield}}/4$).

Table 5 Initial stress-dependent creep time limits and relative deviations of calculated creep compliances from measured ones

Composites	Stress MPa	Creep time limit $t_{\text{limit},\parallel}$ s	Creep time limit $t_{\text{limit},\perp}$ s	Relative deviation of calculated compliance $\Delta J_{\text{rel},\parallel}$ to time $t_{\text{limit},\parallel}$ %	Relative deviation of calculated compliance $\Delta J_{\text{rel},\perp}$ to time $t_{\text{limit},\perp}$ %
PBT GF20 CIM	12.5	614072	350825	28.0	4.5
	25	23321	2905	27.5	3.4
	37.5	535	220	28.1	5.8
PBT GF20 PPP	12.5	>1217441	441259	37.9	16.4
	25	56666	350615	34.7	16.7
	37.5	535	1220	34.5	16.3
PBT GF30 CIM	12.5	441259	>1217441	11.9	5.5
	25	56666	12310	9.5	2.1
	37.5	220	535	10.4	3.3
PBT GF30 PPP	12.5	23535*	614072	32.9	12.0
	25	36225	23321	34.1	8.9
	37.5	844	387	33.9	12.0

* $t_{\text{limit},\parallel}$ is determined too small because the measured creep compliance curve exhibits a small shift to slightly reduced values at creep times of 10,000 s, 23,535 s, and 221,926 s; correction of these shifts leads to $t_{\text{limit},\parallel} =$ 614072 s.

Table 6 Fit parameters a_1 and a_0 due to equation (35) parallel and perpendicular to the flow direction with correlation coefficients

Composites	Fibers ∥ flow direction			Fibers ⊥ flow direction		
	$a_{1,\parallel}$ MPa	$a_{0,\parallel}$ MPa	Correlation coefficient	$a_{1,\perp}$ MPa	$a_{0,\perp}$ MPa	Correlation coefficient
PBT GF20 CIM	−8,16	60,0	0,998	−7,58	53,7	0,971
PBT GF20 PPP	−7,35	58,2	0,986	−7,61	61,2	0,779
PBT GF30 CIM	−7,07	55,0	0,934	−7,36	56,7	0,988
PBT GF30 PPP	−8,68	63,4	0,993	−7,78	58,0	0,996

4 Conclusions

Fiber orientation and aspect ratio affect the stiffness and creep compliance of short-fiber-reinforced PBT composites. The EV approach takes into account them and predicts systematically too small but still sufficiently accurate creep compliances based on matrix creep. It also allows for the expression of shear creep in terms of the transverse creep necessary in cases of misalignment of fiber orientation. This underprediction is a result of the assumption *perfect fiber matrix adhesion* and *pure elasticity of the composite part of the EV*. It has to be emphasized that the model holds for any temperature not too close to glass transition temperatures as matrix properties become strongly time and stress dependent. SEM images of fracture surfaces show that the fiber-matrix adhesion is good but not perfect. Furthermore, it seems that different adhesion mechanisms act at the interface depending on the stress direction with respect to the fiber axes. This requires further research if adhesion is introduced

to the creep compliance relations as a further material property. However, the EV approach opens, in principle, a way to express fiber-matrix adhesion in terms of an adhesion factor that can be quantified using a final fit procedure. The 2D consideration based on RM Jones' assumption of a *plane stress state* works well for the thin plates investigated in this study. However, for thicker and more complex parts, the fiber orientation must be considered by a 3D calculation using the components of the orientation tensor.

Supplementary information The online version contains supplementary material available at https://doi.org/10.1007/s11043-025-09801-z.

Author contributions CRediT authorship contribution statement J. Rech: Conceptualization, Methodology, Validation, Formal analysis, Writing – Original Draft, Writing – Review and Editing, Investigation, Data curation, Visualization. B. Möginger: Conceptualization, Methodology, Resources, Writing – Review and Editing, Supervision. H.C. Ludwig: Conceptualization, Methodology, Resources. B. Hausnerova: Conceptualization, Writing – Review and Editing, Supervision.

Funding information Open access publishing supported by the institutions participating in the CzechELib Transformative Agreement.

Data availability Data Access Statement: Research data supporting this publication are available from the NN repository at located at www.NNN.org/download/.

Declarations

Ethical compliance All procedures performed in studies involving human participants were in accordance with the ethical standards of the institutional and/or national research committee and with the 1964 Helsinki Declaration and its later amendments or comparable ethical standards.

Competing interests The authors declare no competing interests.

References

Amjadi, M., Fatemi, A.: Creep behavior and modeling of high-density polyethylene (HDPE). Polym. Test. **94**, 107031 (2021). https://doi.org/10.1016/j.polymertesting.2020.107031

BASF, Ultradur® (PBT) Hauptbroschüre (main brochure)

Breuer, K., Stommel, M.: RVE modelling of short fiber reinforced thermoplastics with discrete fiber orientation and fiber length distribution. SN Appl. Sci. **2**(91) (2020). https://doi.org/10.1007/s42452-019-1890-5

Chin, W.K., Liu, H.T., Lee, Y.D.: Effects of fiber length and orientation distribution on the elastic modulus of short fiber reinforced thermoplastics. Polym. Compos. **9**(1), 27–35 (1988). https://doi.org/10.1002/pc.750090105

Dean, G., McCartney, N., Crocker, L., Mera, R.: Modelling the Long-term Deformation Behaviour of Polymers for Finite Element Analysis. NPL REPORT MAT 22 (2008)

Duan, X., Yuan, H., Tang, W., He, J., Guan, X.: A phenomenological primary–secondary–tertiary creep model for polymer-bonded composite materials. Polymers **13**, 2353 (2021). https://doi.org/10.3390/polym13142353

Ediger, B.: Influence of particle geometry on the behavior of composites having nonlinear viscoelastic properties – demonstrated at filled and reinforced polypropylene (in German), thesis Uni Stuttgart (1986)
Eshelby, J.D.: The determination of the elastic field of an ellipsoidal inclusion, and related problems. Proc. R. Soc. Lond. A **241**(1226), 376–396 (1957). https://doi.org/10.1098/rspa.1957.0133
Fliegener, S., Hohe, J., Gumbsch, P.: The creep behavior of long fiber reinforced thermoplastics examined by microstructural simulations. Compos. Sci. Technol. **131**(2), 1–11 (2016). https://doi.org/10.1016/j.compscitech.2016.05.006
Fu, S.Y.: Effects of fiber length and fiber orientation distributions on the tensile strength of short-fiber-reinforced polymers. Compos. Sci. Technol. **56**(10), 1179–1190 (1996). https://doi.org/10.1016/S0266-3538(96)00072-3
Gates, T.S., Veazie, D.R., Brinson, C.: A Comparison of Tension and Compression Creep in a Polymeric Composite and the Effects of Physical Aging on Creep. NASA Technical Memorandum, vol. 110273, (1996)
Gusev, A.A.: J. Mech. Phys. Solids **45**, 1449 (1997). https://doi.org/10.1016/S0022-5096(97)00016-1
Gusev, A.A.: Macromolecules **34**, 3081 (2001)
Halpin, J.C., Kardos, J.L.: The Halpin–Tsai equations: a review. Polym. Eng. Sci. **16**(5), 344–352 (1976). https://doi.org/10.1002/pen.760160512
Hermans, J.J.: Proc. Kon. Ned. Akad. v. Wetensch. B **65**, 1 (1967)
Hill, R.: Theory of mechanical properties of fibre-strengthened materials: I. elastic behavior. J. Mech. Phys. Solids **12**(4), 199–212 (1964). https://doi.org/10.1016/0022-5096(64)90019-5
Jones, R.M.: Mechanics of Composite Materials. ISBN 12 978-0070327900, pp. 45–57. Taylor & Francis Inc, London (1975)
Katouzian, M., Vlase, S., Marin, M., Luminita Scutaru, M.: Modeling study of the creep behavior of carbon fiber reinforced composites: a review. Polymers **15**, 194 (2023). https://doi.org/10.3390/polym15010194
Kech, A., Ludwig, H.C., Möginger, B., Eyerer, P., de Claville Christiansen, J.: Mechanical properties of isotactic polypropylene with oriented and cross-hatched lamellae structure. Int. Polym. Process., 202–207 (2000). https://doi.org/10.3139/217.1588
Kojima, S.: Poisson's ratio of glasses, ceramics, and crystals. Materials **17**, 300 (2024). https://doi.org/10.3390/ma17020300
Lim, S.D., Rhee, J.M., Nah, C., Lee, S.H., Lyu, M.Y.: Predicting the Long-term Creep Behavior of Plastics Using the Short-term Creep Test. Int. Polym. Process. XIX(3), IPP_ipp_2004_03_1826 – 20.7.04/druckhaus (2004)
Ludwig, H.C.: Push pull processing – a new processing technique to optimize materials properties of reinforced and neat thermoplastics (in German). Thesis Uni Stuttgart (1998)
Lusti, H.R.: Property Predictions for Short Fiber and Platelet Filled Materials by Finite Element Calculations. (2003), DISS. ETH NO. 15078
Möginger, B.: Effects of processing on morphology and deformation behavior of poly(butylene terephthalate, PBT). Thesis, Uni Stuttgart (1992). (In German)
Möginger, B., Ludwig, H.C., Kech, A., Eyerer, P.: Berechnung mechanischer Kenngrößen von Kurzfaserverbunden mit dem Elementar-Volumen-Konzept. KGK, Kautsch. Gummi Kunstst. 52 Jahrgang Nr. 3/99 (1999)
Mori, T., Tanaka, K.: Average stress in matrix and average elastic energy of materials with misfitting inclusions. Acta Metall. Mater. **21**(5), 571–574 (1973). https://doi.org/10.1016/0001-6160(73)90064-3
Naumann, T., Stommel, M.: Simulation of the long term behavior of polymers on the basis of short term data. Tech. Mech. **32**(2-5), 446–462 (2012)
Pöllet, P.: Automatisierte Zeitstandsmessung – Verfahren mit berührungsloser Dehnungsmessung. Kunststoffe **75**, 829–834 (1985)
Qiu, Y.P., Weng, G.J.: On the application of Mori–Tanaka's theory involving transversely isotropic spheroidal inclusions. Int. J. Eng. Sci. **28**(11), 1121–1137 (1990). https://doi.org/10.1016/0020-7225(90)90112-V
Rauter, N., Lammering, R.: Correlation structure in the elasticity tensor for short fiber reinforced composites. Probab. Eng. Mech. **62**(10) (2020). https://doi.org/10.1016/j.probengmech.2020.103100
Rech, J., Ramakers-van Dorp, E., Michels, P., Möginger, B., Hausnerova, B.: Introduction of an adhesion factor to cube in cube models and its effect on calculated moduli of particulate composites. Sci. Rep. **12**, 16225 (2022a). https://doi.org/10.1038/s41598-022-20629-2
Rech, J., Ramakers-van Dorp, E., Möginger, B., Hausnerova, B.: Modeling of creep behavior of particulate composites with focus on interfacial adhesion effect. Int. J. Mol. Sci. **23**, 14120 (2022b). https://doi.org/10.3390/ijms232214120
Sakai, T., Hirai, Y., Somiya, S.: Estimating the creep behavior of glass fiber reinforced polyamide considering the effects of crystallinity and fiber volume fraction. Mech. Adv. Mater. Mod. Process. **4**, 5 (2018). https://doi.org/10.1186/s40759-018-0038-4

Tandon, G.P., Weng, G.J.: The effect of aspect ratio of inclusions on the elastic properties of unidirectionally aligned composites. Polym. Compos. **5**(4), 327–333 (1984). https://doi.org/10.1002/pc.750050413

Tucker, C.L. III, Liang, E.: Stiffness predictions for unidirectional short fiber composites: review and evaluation. Compos. Sci. Technol. **59**(5), 655–671 (1999). https://doi.org/10.1016/S0266-3538(98)00120-1

Wilczynski, A.R.: A basic theory of reinforcement for unidirectional fibrous composites. Compos. Sci. Technol. **38**, 327–337 (1990). https://doi.org/10.1016/0266-3538(90)90019-2

Wire, S.L., Duckett, R.A., Hine, P.J., Ward, I.M.: Elastic property estimates of a unidirectional discontinuous fibre composite. Compos. Sci. Technol. **59**, 113–122 (1999). https://doi.org/10.1016/S0266-3538(98)00057-8

Zhai, Z.Y., Jiang, B.Y., Drummer, D.: Tensile creep behavior of quasi-unidirectional E-glass fabric reinforced polypropylene composite. Polymers **10**, 661 (2018). https://doi.org/10.3390/polym10060661

Zhang, Y.Y., Sun, Z., Li, Y.Q., Huang, P., Chen, Q., Fu, S.Y.: Tensile creep behavior of short-carbon-fiber reinforced polyetherimide composites. Composites, Part B, Eng. **212**, 108717 (2021). https://doi.org/10.1016/j.compositesb.2021.108717